Electronic Supporting Information for

Luminescent halogen-substituted 2-(*N*-arylimino)pyrrolyl boron complexes: the internal heavy atom effect

Ana I. Rodrigues,[a] Paramasivam Krishnamoorthy,[a,h] Clara S. B. Gomes,[a,i,j] Nicolas Carmona,[a] Roberto E. Di Paolo,[a] Piotr Pander,[c] João Pina,[d] J. Sérgio Seixas de Melo,[d] Fernando B. Dias,[c] Maria José Calhorda,[e] António L. Maçanita,[a,b] Jorge Morgado[f,g] and Pedro T. Gomes*[,a,b]

[a] *Centro de Química Estrutural, Instituto Superior Técnico, Universidade de Lisboa, Av. Rovisco Pais, 1049-001 Lisboa, Portugal.*

[b] *Departamento de Engenharia Química, Instituto Superior Técnico, Universidade de Lisboa, Av. Rovisco Pais, 1049-001 Lisboa, Portugal.*

[c] *Department of Physics, Durham University, South Road, Durham DH1 3LE, United Kingdom.*

[d] *University of Coimbra, Coimbra Chemistry Centre, Department of Chemistry, Rua Larga, 3004-535 Coimbra, Portugal.*

[e] *BioISI -Biosystems & Integrative Sciences Institute, Departamento de Química e Bioquímica, Faculdade de Ciências, Universidade de Lisboa, Campo Grande, Ed. C8, 1749-016 Lisboa, Portugal.*

[f] *Instituto de Telecomunicações, Av. Rovisco Pais, 1049-001 Lisboa, Portugal.*

[g] *Department of Bioengineering, Instituto Superior Técnico, Universidade de Lisboa, Av. Rovisco Pais, 1049-001 Lisboa, Portugal.*

[h] *Centre for Environmental Research, Department of Chemistry, Kongu Engineering College, Perundurai, Erode 638 060, India*

[i] *LAQV-REQUIMTE, Departamento de Química, Faculdade de Ciências e Tecnologia, Universidade NOVA de Lisboa, 2829-516, Caparica, Portugal.*

[j] *UCIBIO-REQUIMTE, Departamento de Química, Faculdade de Ciências e Tecnologia, Universidade NOVA de Lisboa, 2829-516 Caparica, Portugal.*

* Corresponding author: Pedro T. Gomes; E-mail: pedro.t.gomes@tecnico.ulisboa.pt

Table of Contents

Crystallographic and molecular structure data of boron complexes 4c, 4d and 4g

Table S1. Crystallographic data for boron complexes **4c**, **4d**, and **4g**.

	4c	**4d**	**4g**
Formula	$C_{23}H_{18}BClN_2$	$C_{23}H_{18}BBrN_2$	$C_{23}H_{18}BBrN_2$
M (g mol^{-1})	368.65	413.11	413.11
λ (Å)	0.71073	0.71073	0.71073
T (K)	150(2)	150(2)	150(2)
Crystal system	Triclinic	Triclinic	Triclinic
Space group	*P*-1	*P*-1	*P*-1
a (Å)	9.8331(9)	9.881(2)	13.7466(7)
b (Å)	10.4055(10)	10.408(2)	15.6514(8)
c (Å)	11.3375(10)	11.328(3)	18.1015(9)
α (º)	102.953(5)	75.691(11)	97.133(3)
β (º)	104.742(5)	76.723(10)	96.005(3)
γ (º)	113.592(4)	82.882(11)	91.090(3)
V (Å^3)	956.00(16)	1095.8(4)	3841.2(3)
Z	2	2	8
ρ_{calc} (g cm^{-3})	1.281	1.252	1.429
μ (mm^{-1})	0.209	1.884	2.150
Crystal size	0.50×0.10×0.10	0.20×0.08×0.06	0.40×0.40×0.26
Crystal color	Yellow	Yellow	Colorless
Crystal description	Prism	Prism	Block
θ_{max} (º)	26.491	25.681	28.368
Total data	12625	10877	56275
Unique data	3887	3944	19018
R_{int}	0.0412	0.0807	0.0644
$R[I>2\sigma(I)]$	0.0386	0.0583	0.0482

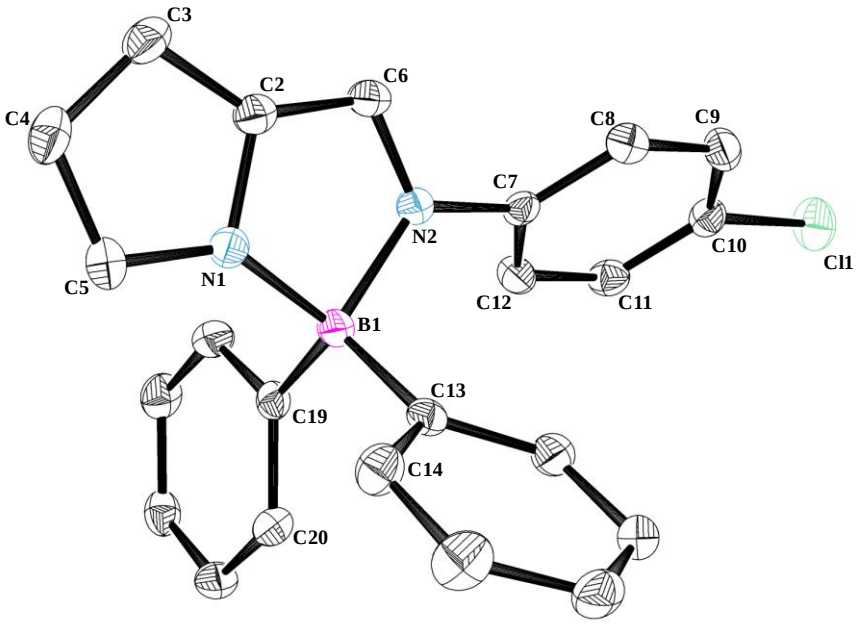

Figure S1. Perspective view of 2-iminopyrrolyl-BPh_2 complex **4c**. The calculated hydrogen atoms were omitted for clarity and the ellipsoids were drawn at the 50% probability level. Complex **4c**: selected bond distances (Å): Cl1-C10, 1.739(2); N2-C6, 1.315(2); N2-C7, 1.429(2); N2-B1, 1.631(2); N1-C5, 1.345(2); N1-C2, 1.376(2); N1-B1, 1.565(2); C2-C3, 1.395(2); C2-C6, 1.403(2); C3-C4, 1.385(2); C4-C5, 1.393(2); C7-C12, 1.384(2); C7-C8, 1.388(2); C8-C9, 1.380(2); C9-C10, 1.379(2); C10-C11, 1.380(2); C11-C12, 1.386(2); C13-C14, 1.399(2); C13-B1, 1.609(2); C19-C20, 1.397(2); C19-B1, 1.620(2). Selected bond angles (º): C6-N2-C7, 121.57(13); C6-N2-B1, 111.02(12); C7-N2-B1, 127.23(12); C5-N1-B1, 139.73(14); C2-N1-B1, 112.46(12); N1-C2-C3, 109.26(14); N1-C2-C6, 109.02(13); C3-C2-C6, 141.37(16); C4-C3-C2, 106.19(15); C3-C4-C5, 107.64(14); N1-C5-C4, 109.35(15); N2-C6-C2, 112.40(14); C12-C7-C8, 119.96(14); C12-C7-N2, 120.90(14); C8-C7-N2, 119.13(13); C9-C8-C7, 120.15(15); C8-C9-C10, 119.28(15); C9-C10-C11, 121.39(15); C9-C10-Cl1, 118.77 (13); C11-C10-Cl1, 119.84(12); C10-C11-C12, 119.13(15); C7-C12-C11, 120.07(15); C14-C13-B1, 121.49(14); C20-C19-B1, 123.11(14); N1-B1-C13, 109.99(12); N1-B1-C19, 112.26(13); C13-B1-C19, 115.51(13); N1-B1-N2, 94.92(12); C13-B1-N2, 113.33(12); C19-B1-N2, 109.04(12).

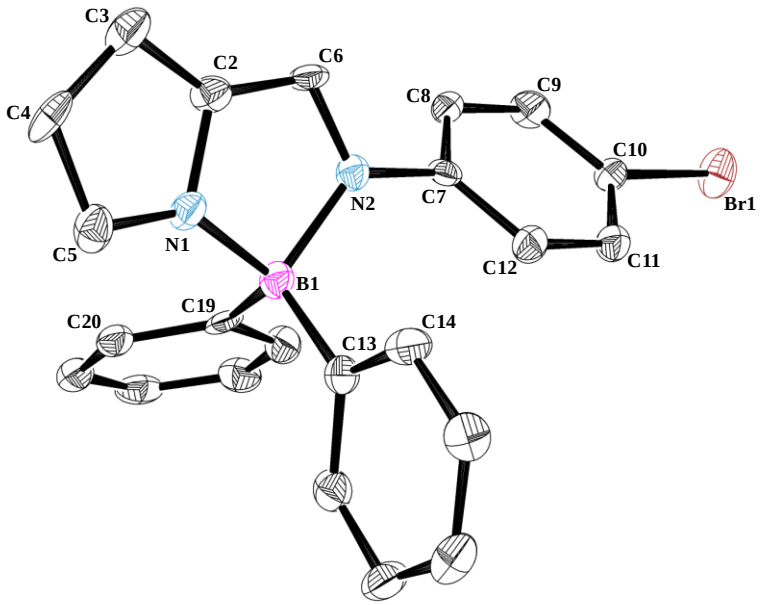

Figure S2. Perspective view of 2-iminopyrrolyl-BPh_2 complex **4d**. The calculated hydrogen atoms were omitted for clarity and the ellipsoids were drawn at the 50% probability level. Selected bond distances (Å): Br1-C10, 1.890(5); N1-C5, 1.329(6); N1-C2, 1.384(7); N1-B1, 1.566(6); N2-C6, 1.323(6); N2-C7, 1.434(6); N2-B1, 1.634(7); C2-C61.396(7); C2-C3, 1.389(7); C3-C4, 1.383(8); C4-C5, 1.405(7); C7-C8, 1.380(7); C7-C12, 1.398(7); C8-C9, 1.388(7); C9-C10, 1.389(7); C10-C11, 1.387(7); C11-C12, 1.377(7); C13-C14, 1.392(7); C13-B1, 1.611(7); C19-C20, 1.405(7); C19-B1, 1.613(7). Selected bond angles (º): C5-N1-C2, 108.1(4); C5-N1-B1, 139.5(5); C2-N1-B1, 112.2(4); C6-N2-C7, 120.9(4); C6-N2-B1, 111.3(4); C7-N2-B1, 127.5(4); N1-C2-C6, 109.6(4); N1-C2-C3, 108.9(5); C6-C2-C3, 141.4(5); C4-C3-C2, 106.4(5); C3-C4-C5, 107.4(5); N1-C5-C4, 109.1(5); N2-C6-C2, 111.9(5); C8-C7-C12, 120.5(4); C8-C7-N2, 121.0(4); C12-C7-N2, 118.5(4); C7-C8-C9, 120.2(4); C10-C9-C8, 119.0(5); C11-C10-C9, 120.9(4); C11-C10-Br1, 119.4(4); C9-C10-Br1, 119.7(4); C12-C11-C10, 119.8(5); C11-C12-C7, 119.6(5); C14-C13-B1, 121.6(5); C20-C19-B1, 123.3(4); N1-B1-C19, 111.6(4); N1-B1-C13, 110.5(4); C19-B1-C13, 116.3(4); N1-B1-N2, 94.8(4); C19-B1-N2, 108.3(4); C13-B1-N2, 113.3(4).

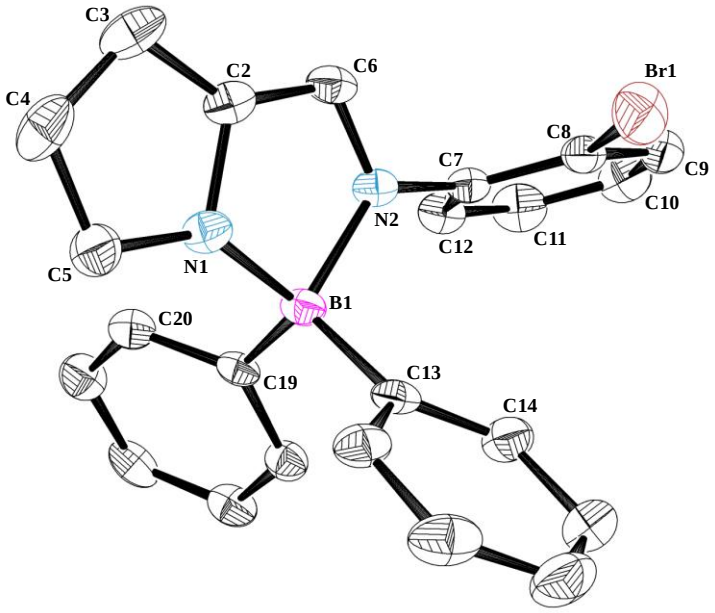

Figure S3. Perspective view of 2-iminopyrrolyl-BPh_2 complex **4g** (molecule A). The calculated hydrogen atoms were omitted for clarity and the ellipsoids were drawn at the 50% probability level. Selected bond distances (Å): Br1A-C8A, 1.891(3); N1A-C5A, 1.346(3); N1A-C2A, 1.380(3); N1A-B1A, 1.558(4); N2A-C6A, 1.304(3); N2A-C7A, 1.429(3); N2A-B1, 1.627(3); C2A-C3A, 1.387(4); C2A-C6A, 1.402(3); C3A-C4A, 1.386(4); C4A-C5A, 1.385(4); C7A-C12A, 1.383(3); C7A-C8A, 1.397(3); C8A-C9A, 1.388(3); C9A-C10A, 1.371(4); C10A-C11A, 1.376(4); C11A-C12A, 1.388(3); C13A-C14A, 1.401(4); C13A-B1A, 1.601(4); C19A-C20A, 1.401(3); C19A-B1A, 1.609(4). Selected bond angles (º): C5A-N1A-C2A, 107.0(2); C5A-N1A-B1A, 140.3(2); C2A-N1A-B1A, 112.46(19); C6A-N2A-C7A, 121.14(19); C6A-N2A-B1A, 111.38(19); C7A-N2A-B1A, 127.5(2); N1A-C2A-C3A, 109.8(2); N1A-C2A-C6A, 108.7(2); C3A-C2A-C6A, 141.2(3); C2A-C3A-C4A, 105.7(2); C5A-C4A-C3A, 108.1(2); N1A-C5A-C4A, 109.4(2); N2A-C6A-C2A, 112.5(2); C12A-C7A-C8A, 119.2(2); C12A-C7A-N2A, 118.9(2); C8A-C7A-N2A, 121.9(2); C9A-C8A-C7A, 119.7(2); C9A-C8A-Br1A, 119.1(2); C7A-C8A-Br1A, 121.22(19); C10A-C9A-C8A, 120.1(3); C11A-C10A-C9A, 120.9(3); C10A-C11A-C12A, 119.3(3); C7A-C12A-C11A, 120.7(2); C14A-C13A-B1A, 122.5(2); C20A-C19A-B1A, 120.1(2); N1A-B1A-C13A, 112.2(2); N1A-B1A-C19A, 110.4(2); C13A-B1A-C19A, 116.9(2); N1A-B1A-N2A, 94.86(18); C13A-B1A-N2A, 109.35(19); C19A-B1A-N2A, 111.0(2).

Fluorescence and transient-absorption of complex 4h

The fluorescence decay of **4h** in THF required a sum of three exponentials to be fitted (Fig. S4): two short decay-times with large pre-exponential coefficients and a long decay-time with small pre-exponential coefficient. The possibility that the fastest decay-time (27 ps) would be due to light scattering was discarded based on the bad fit obtained from analysis with two exponentials plus the experimental IRF (Sand program option). Therefore, we attribute this result to the presence of some fast photoreaction occurring with **4h** (but not with the similar **4g**) eventually related to the contribution of the p(I)→π*transition in the singlet excited state.

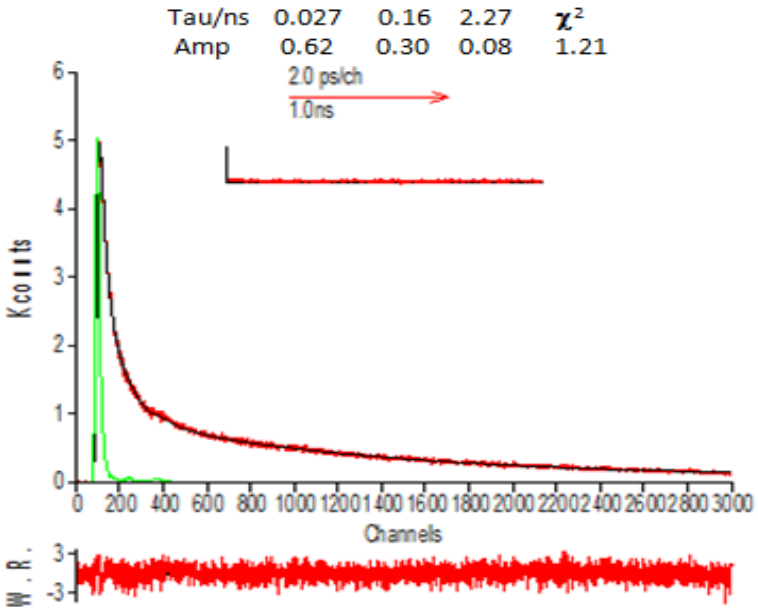

Figure S4. Triexponential fit (red) of the fluorescence decay (black) of iminopyrrolyl boron complex **4h** in THF solution at 298 K, showing the decay times (Tau), pre-exponential coefficients (Amp), chi-squared value (χ^2), autocorrelation function (A.C.) and weighted residuals (W.R.). The impulse response function (IRF) is shown in green.

In order to evaluate approximate values for the rate constants k_f and k_{nr}, we have calculated the average decay-time ($\tau_{average}=\Sigma A_i \tau_i^2/\Sigma A_i \tau_i$) considering the three exponential terms (i=3) and obtained $\tau_{average}$= 1.72 ns. With this time, we obtained $k_f = \Phi_f/\tau_{average}$= 0.006 ns^{-1}, a value more than one order of magnitude lower than those of the other complexes, which is difficult to justify. Moreover, the value of k_{nr} = 0.58 ns^{-1} is similar to those of the other complexes, which is not compatible with the contribution of the photoreaction rate constant ($k_{reaction}$) in $k_{nr}= k_{ic}+k_{isc}+k_{reaction}$. On the other hand, when $\tau_{average}$ is assumed equal to the average time of

the two shortest decay times ($\tau_{average}=\Sigma A_i \tau_i^2/\Sigma A_i \tau_i$ = 0.13 ns), the k_f = 0.08 ns^{-1} value is similar to that of complex **4g** (k_f = 0.09 ns^{-1}) and $k_{nr} = k_{ic}+k_{isc}+k_{reaction}$ = 7.66 ns^{-1} is consistent with the presence of the photoreaction.

The presence of two decay times indicates reversibility of the photoreaction, such as reversible fragmentation followed by diffusion-controlled separation of the resulting fragments (*e.g.*, homolytic cleavage of the iodine-C bond followed by separation of the resulting radicals). The longest decay time (2.27 ns) may be due to the emission of some photoproduct accumulated during the very long time of the measurement and absorbing at the excitation wavelength. Such photoproduct would be negligibly formed during the much faster measurement of the fluorescence spectrum.

The transient absorption spectrum of **4h** at 8 μs (Fig. S5a) shows the expected depletion (ΔA<0) in the 310-420 nm, mirroring its absorption spectrum (Fig. 2, right bottom), and the absorption of triplets (ΔA>0) above 380 nm. However, the time-dependence of ΔA, within the depletion wavelength range, required a sum of two exponential terms plus a constant to be fitted, contrary to that of the other complexes (single-exponentials). For longer wavelengths acceptable fits were obtained with a single exponential plus a constant (Fig. S5b). These observations (multiexponentials and the presence of a constant) clearly imply the presence of the photoreaction.

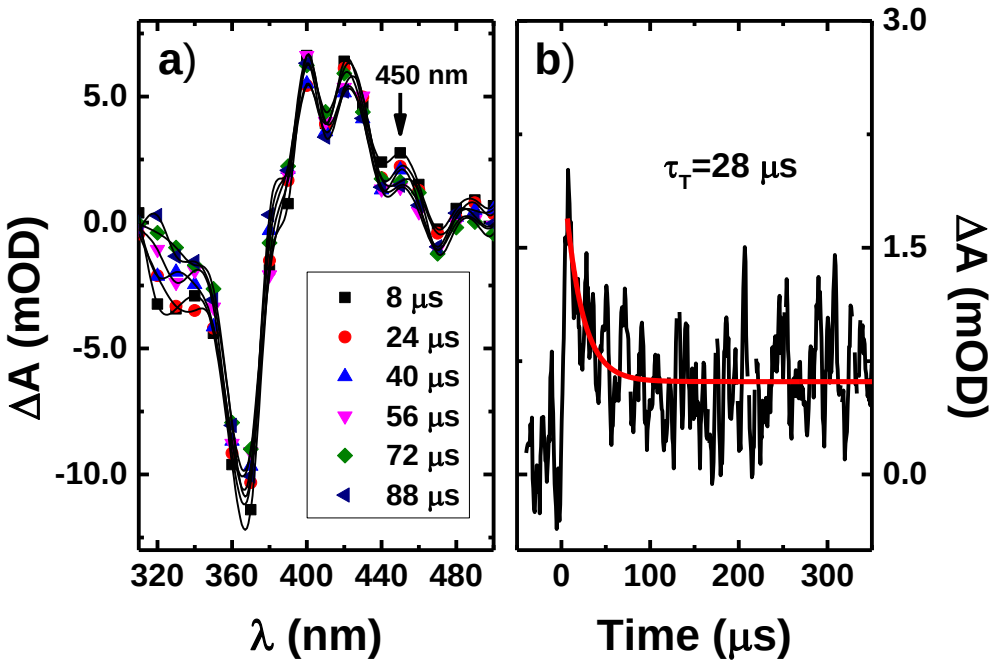

Figure S5. Room temperature (a) time-resolved transient absorption spectra, together with the (b) representative kinetic trace (and fit) collected at 450 nm for complex **4h** in THF.

Computational studies

Table S2. Calculated (DFT) dihedral angles (°) for complexes **4a**-**4h** in the ground and first singlet excited state using different methods.

	Ground state					First singlet excited state					First triplet excited state				
	GP	A	B	A/D3	B/D3	GP	A	B	A/D3	B/D3	GP	A	B	A/D3	B/D3
Angle	C6-N2-C7-C8														
4a	29	35	36	36	38	2	3	5	2	4	3	3	5	2	4
4b	-31	-38	-40	-40	-42	-3	-1	-1	1	-1	na	-2	-2	-1	-1
4c	36	36	36	36	36	2	1	2	2	2	2	2	2	1	2
4d	-36	-37	-39	-38	-40	-3	-1	1	-1	0	-3	-1	0	-1	0
4e	-36	-36	-38	-38	-38	-3	-1	0	-1	0	-3	-2	0	-1	0
4f	-37	-39	-36	-39	-36	-3	-2	-2	-1	-2	-3	-2	-3	-2	-2
4g	54	59	59	61	61	24	29	45	24	24	25	32	31	32	31
4h	-54	-58	-57	-61	-62	-21	-66	-46	-21	-20	-29	-30	-26	-29	-28

A – PBE0, TZP (all electron), THF, SO
A/D3 – PBE0/D3, TZP (all electron), THF, SO
B – B3LYP, TZP (all electron), THF, SO
B/D3 – B3LYP/D3, TZP (all electron), THF, SO
GP – BP86 (small core, TZ2P)

Table S3. Calculated HOMOs and LUMOS energies (eV) for complexes **4a**-**4h** using different methods.

	A		A/D3		B		B/D3		GP		THF		CH_2Cl_2	
	HOMO	LUMO	HOMO	LUMO	HOMO	LUMO	HOMO	LUMO	HOMO	LUMO	HOMO	LUMO	HOMO	LUMO
4a	-6.346	-2.122	-6.336	-2.096	-6.037	-2.165	-6.028	-2.137	-5.396	-2.933	-5.414	-2.877	-5.511	-2.978
4b	-6.363	-2.098	-6.332	-2.087	-6.064	-2.150	-6.021	-2.126	-5.449	-3.003	-5.406	-2.844	-5.492	-2.975
4c	-6.361	-2.182	-6.357	-2.079	-6.058	-2.232	-6.055	-2.129	-5.632	-3.155	-5.442	-2.895	-5.529	-2.990
4d	-6.360	-2.178	-6.343	-2.160	-6.063	-2.211	-6.038	-2.212	-5.634	-3.158	-5.441	-2.892	-5.522	-2.986
4e	-6.327	-2.172	-6.347	-2.144	-5.669	-2.709	-6.046	-2.181	-5.617	-3.164	-5.414	-2.891	-5.487	-2.984
4f	-6.433	-2.186	-6.316	-2.135	-6.121	-2.267	-6.005	-2.185	-5.705	-3.176	-5.511	-2.912	-5.597	-3.009
4g	-6.498	-2.043	-6.415	-2.161	-6.182	-2.109	-6.100	-2.245	-5.658	-2.996	-5.531	-2.812	-5.618	-2.907
4h	-6.841	-2.044	-6.486	-2.008	-6.158	-2.114	-6.170	-2.069	-5.649	-3.002	-5.556	-2.858	-5.600	-2.906

A – PBE0, TZP (all electron), THF, SO
A/D3 – PBE0/D3, TZP (all electron), THF, SO
B – B3LYP, TZP (all electron), THF, SO
B/D3 – B3LYP/D3, TZP (all electron), THF, SO
GP – BP86 (small core, TZ2P)
THF – BP86 (small core, TZ2P), THF (single point)
CH_2Cl_2 – BP86 (small core, TZ2P), dichloromethane (single point)

Table S4. Calculated energies (eV) of S_1 and T_1 for complexes **4a-4h** using different methods.

	S1					T1				
	A	B	A/D3	B/D3	GP	A	B	A/D3	B/D3	GP
4a	2.729	2.618	2.697	2.597	1.89	1.661	1.637	1.668	1.650	1.72
4b	2.671	2.578	2.671	2.578	1.96	1.639	1.626	1.636	1.621	1.67
4c	2.658	2.552	2.633	2.544	1.84	1.629	1.614	1.648	1.640	1.668
4d	2.646	2.535	2.625	2.531	1.84	1.635	1.611	1.653	1.636	1.673
4e	2.610	2.491	2.592	2.496	1.87	1.633	1.599	1.650	1.595	1.667
4f	2.764	2.652	2.732	2.634	1.91	1.707	1.698	1.706	1.694	1.730
4g	2.832	2.747	2.769	2.679	2.03	1.885	1.966	1.857	1.851	1.866
4h	2.554	2.695	2.637	2.532	2.20	1.863	1.810	1.837	1.825	1.86

A – PBE0, TZP (all electron), THF, SO
A/D3 – PBE0/D3, TZP (all electron), THF, SO
B – B3LYP, TZP (all electron), THF, SO
B/D3 – B3LYP/D3, TZP (all electron), THF, SO
GP – BP86 (small core, TZ2P)

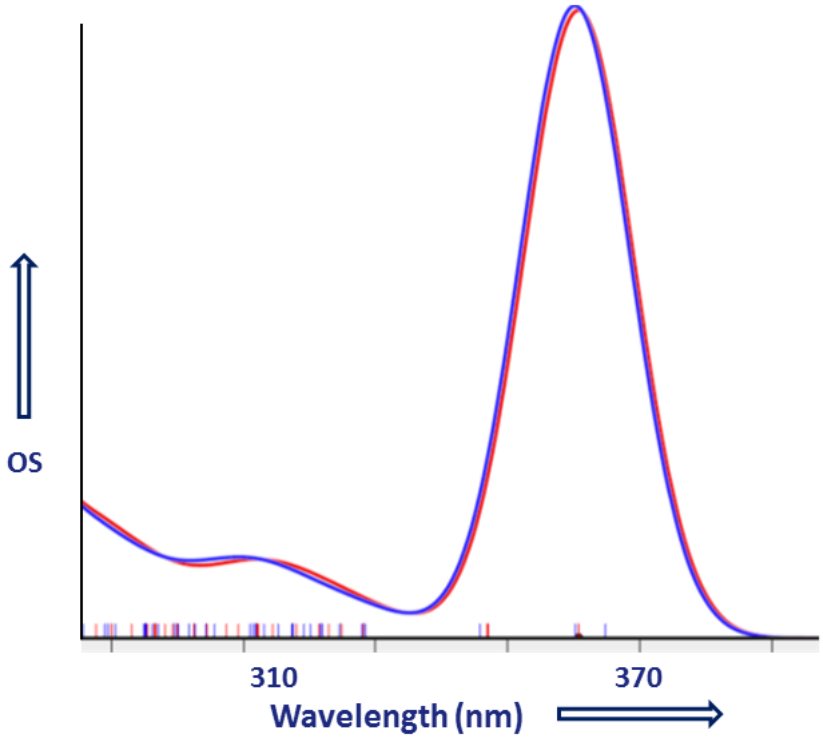

Figure S6. Calculated absorption spectrum of complex **4e**: with SOC (red) and without SOC (blue).

Cyclic Voltammograms of complexes 4c–4h

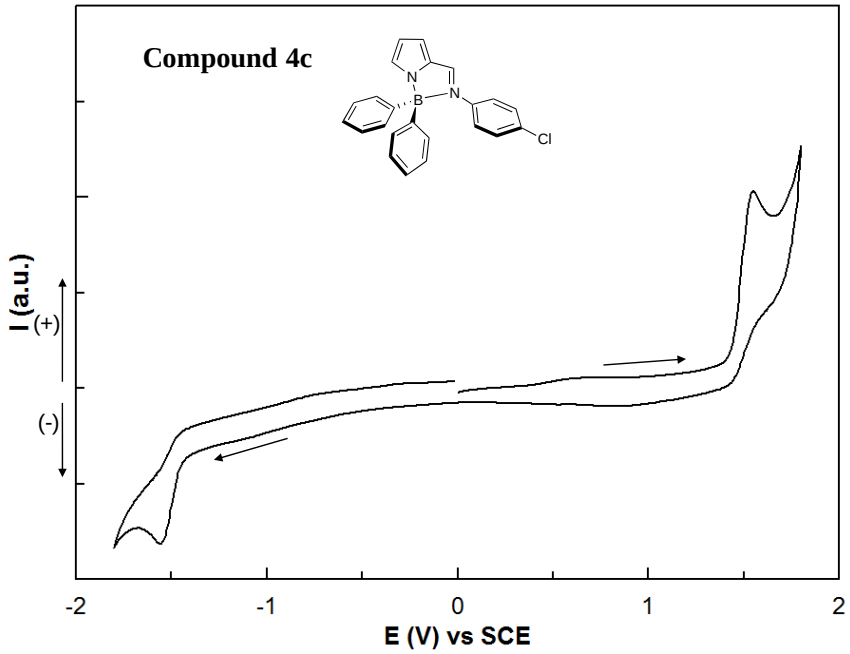

Figure S7. Cyclic voltammogram obtained for complex **4c** at a scan rate of 50 mV/s *versus* SCE (Saturated Calomel Electrode) as the reference electrode. The SCE was calibrated against Fc/Fc^{+} redox couple, for which the measured half-wave potential ($E_{Fc/Fc+}$) was 4.26 eV.

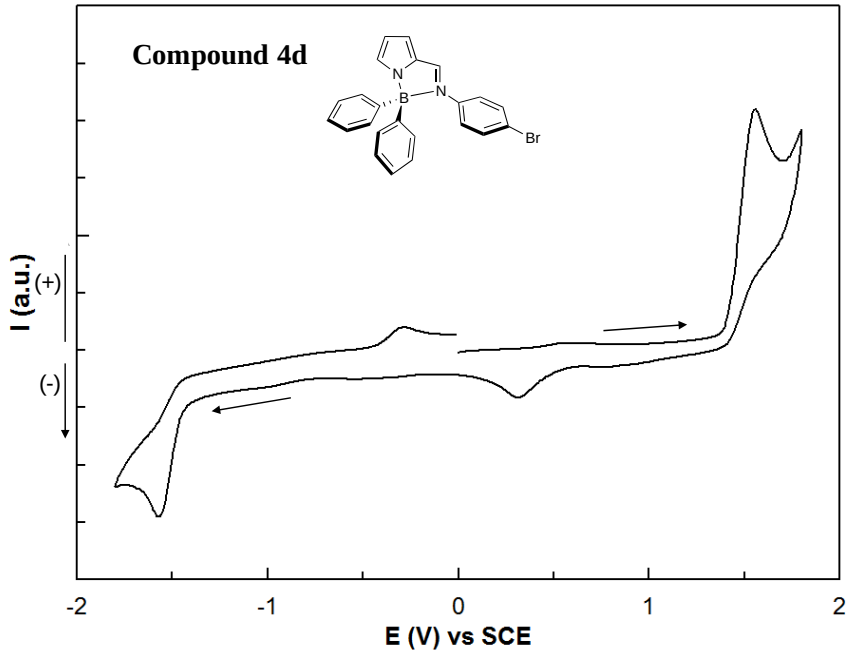

Figure S8. Cyclic voltammogram obtained for complex **4d** at a scan rate of 50 mV/s *versus* SCE, as the reference electrode, calibrated against Fc/Fc^{+} redox couple. The measured half-wave potential ($E_{Fc/Fc+}$) was 4.28 eV.

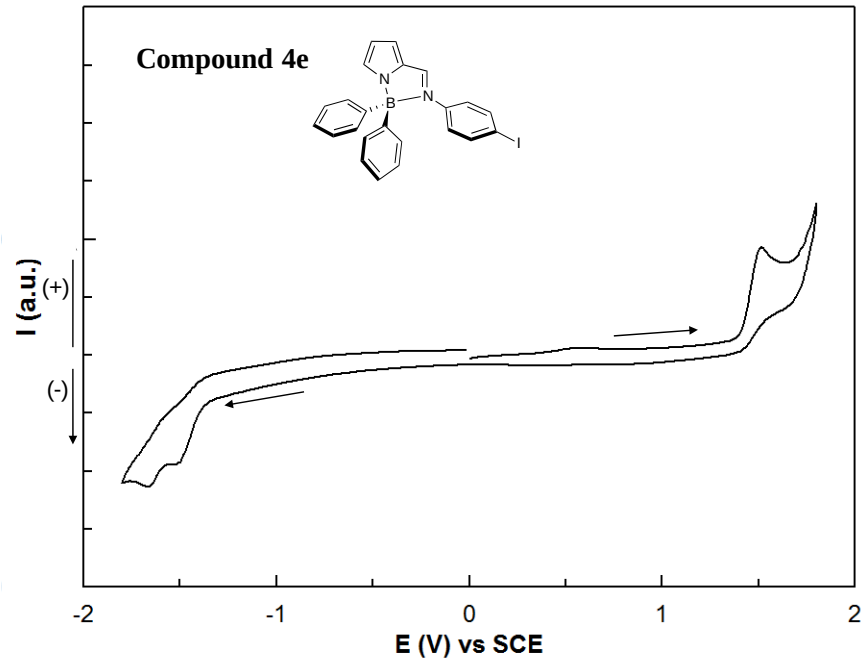

Fig. S9. Cyclic voltammogram obtained for complex **4e** at a scan rate of 50 mV/s *versus* SCE, as the reference electrode, calibrated against Fc/Fc^{+} redox couple. The measured half-wave potential ($E_{Fc/Fc+}$) was 4.26 eV.

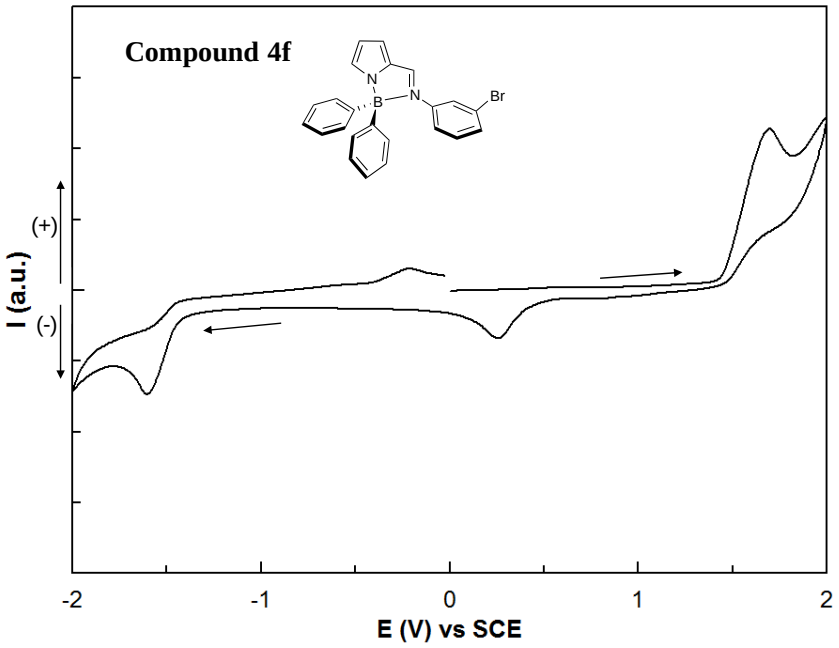

Figure S10. Cyclic voltammogram obtained for complex **4f** at a scan rate of 50 mV/s *versus* SCE, as the reference electrode, calibrated against Fc/Fc^{+} redox couple. The measured half-wave potential ($E_{Fc/Fc+}$) was 4.25 eV.

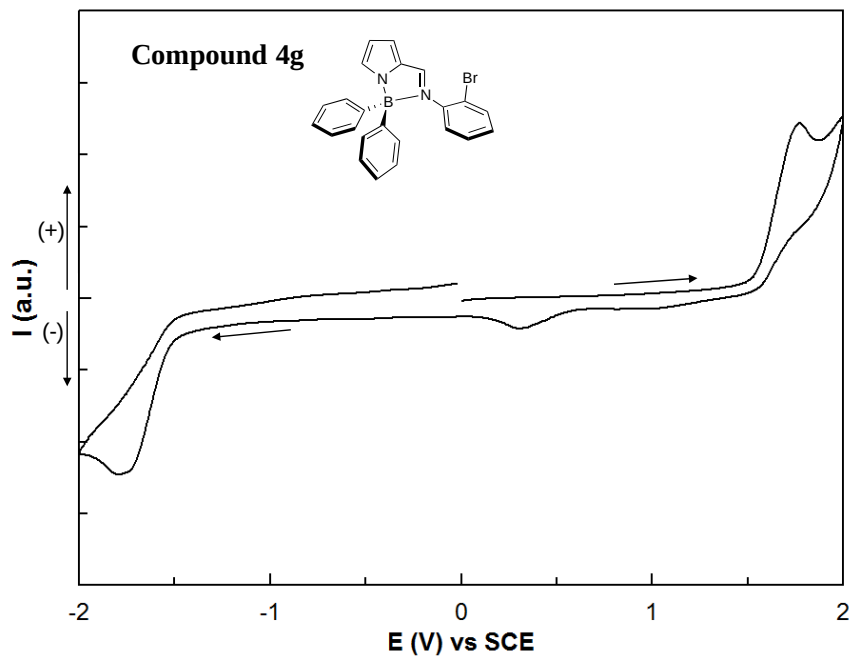

Fig. S11. Cyclic voltammogram obtained for complex **4g** at a scan rate of 50 mV/s *versus* SCE, as the reference electrode, calibrated against Fc/Fc^{+} redox couple. The measured half-wave potential ($E_{Fc/Fc+}$) was 4.25 eV.

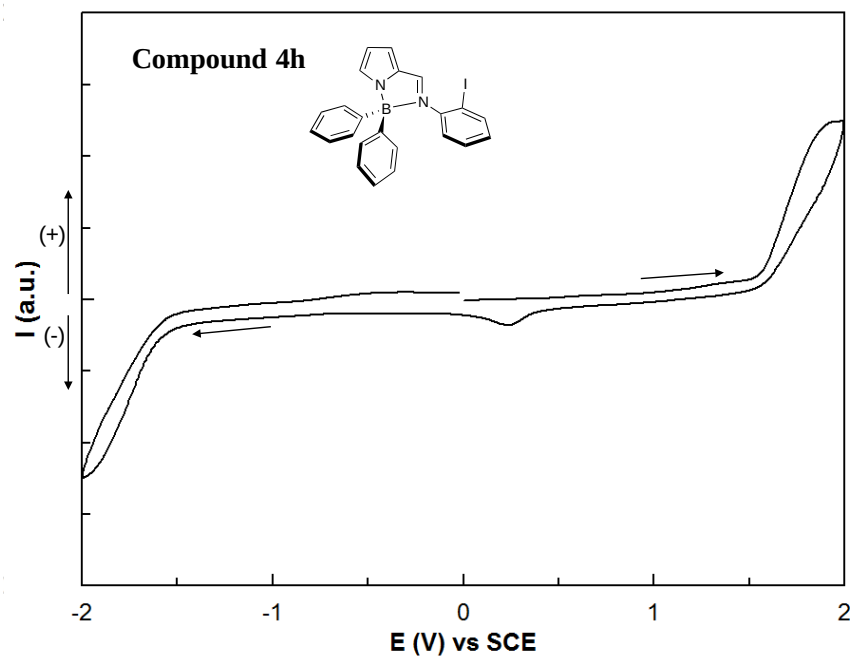

Figure S12. Cyclic voltammogram obtained for complex **4h** at a scan rate of 50 mV/s *versus* SCE, as the reference electrode, calibrated against Fc/Fc^{+} redox couple. The measured half-wave potential ($E_{Fc/Fc+}$) was 4.29 eV.

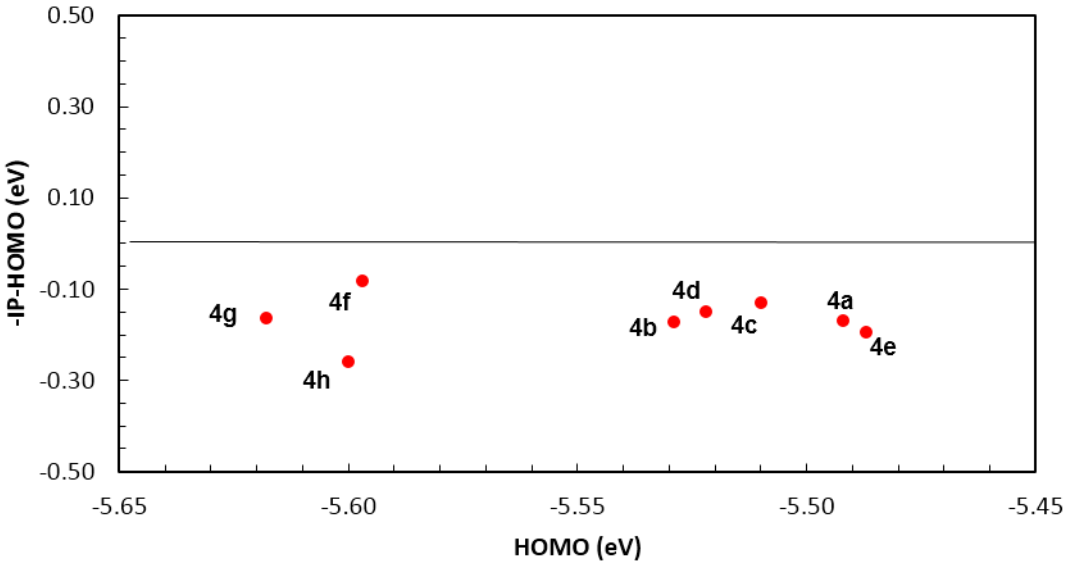

(a)

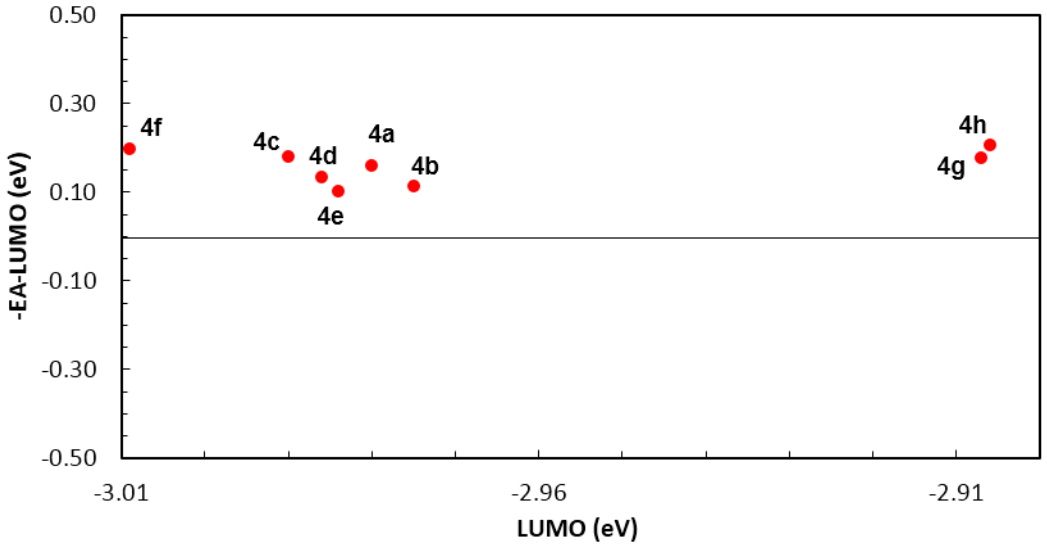

(b)

Figure S13. Plots of (a) the difference between –IP and HOMO versus the energies of the HOMOs, and of (b) the difference between –EA and LUMO versus the energies of the LUMOs of complexes **4a**–**4h**. IP and EA were estimated from cyclic voltammetry measurements, and the energies of the HOMOs and LUMOs were determined by DFT (CH_2Cl_2).

Electroluminescence properties

Light-emitting diodes were prepared on glass/ITO substrates (ITO=indium-tin oxide), which were cleaned with detergent, distilled water, acetone and isopropanol. They were treated with oxygen plasma, prior to the deposition of PEDOT:PSS (poly(3,4-ethylenedioxythiophene) doped with polystyrene sulfonate, CLEVIOS P VP.AI 4083 from Heraeus Clevios GmbH) by spin coating. The PEDOT:PSS films (40 nm thick, as measured with a DEKTAK profilometer) were annealed in air for 2 min at 120 ºC and then, transferred into a nitrogen-filled glove box. The cathodes, consisting of either 1.5 nm LiF or 20 nm Ca and *ca.* 80 nm of aluminium, were deposited at a base pressure of 2×10^{-6} mbar through a shadow mask, defining pixel areas of 4 mm^2.

Films of neat complexes **4c**-**4f** were deposited by spin-coating, inside the glove box, to prepare the following OLEDs structures: ITO (100 nm)/PEDOT:PSS (40 nm)/Complex (*ca.* 80 nm) and ITO (100 nm)/PEDOT:PSS (40 nm)/polyTPD (10 nm)/Complex (*ca.* 80 nm) with a cathode layer of LiF (1.5 nm) or Ca (20 nm), both protected by an overlayer of Al (80-100 nm). PolyTPD (*N*,*N*'-bis(3-methylphenyl)-*N*,*N*'-diphenylbenzidine) was used, in some devices, as the hole-transporting/electron-blocking material. In the case of complexes **4d**, devices with an electron-transporting bathophenanthroline (Bphen) layer were also fabricated and characterized. The results of the devices' performance are shown in Table S5, where the results previously reported for similar OLEDs based on complexes **4a** and **4b** (Ref. 4c) are also shown.

Table S5. Characteristics of OLED devices based on solution-processed neat complexes **4c**-**4f** including luminance maxima (L_{max}, cd m^{-2}), external quantum efficiency (EQE_{max}, %), current efficiency ($\eta_{L_{max}}$, cd A^{-1}), and Commission Internationale de l'Éclairage (CIE) colour coordinates.

Complex	X	L_{max}	EQE_{max}	$\eta_{L_{max}}$	CIE
		ITO/PEDOT:PSS/Complex/Ca/Al			
4a [a]	H	0.4	1.5×10^{-4}	3.8×10^{-4}	0.37, 0.53
4b [a]	4-F	43	2×10^{-3}	2×10^{-3}	0.27, 0.41
		ITO/PEDOT:PSS/Complex/LiF/Al			
4c	4-Cl	22	1.8×10^{-3}	5×10^{-3}	0.22, 0.40
		ITO/PEDOT:PSS/polyTPD/Complex/LiF/Al			
4d	4-Br	24	2×10^{-3}	7×10^{-3}	0.40, 0.53
		ITO/PEDOT:PSS/polyTPD/Complex/Ca/Al			
4e	4-I	4	3×10^{-4}	8×10^{-4}	0.27, 0.46
4f[b]	3-Br	33	1×10^{-3}	3×10^{-3}	0.20, 0.33

[a] Ref. 4c; [b] Active layer thickness of *ca.* 35 nm.

No measurable emission was obtained from the OLEDs prepared by spin coating of complexes **4g** and **4h**. Among the series, **4f**-based OLED showed the maximum luminance of 33 cd m^{-2} with an EQE_{max} of 1×10^{-3}%.

As an example, we show in Figure S14 the characteristics of the device fabricated with **4c** by spin-coating.

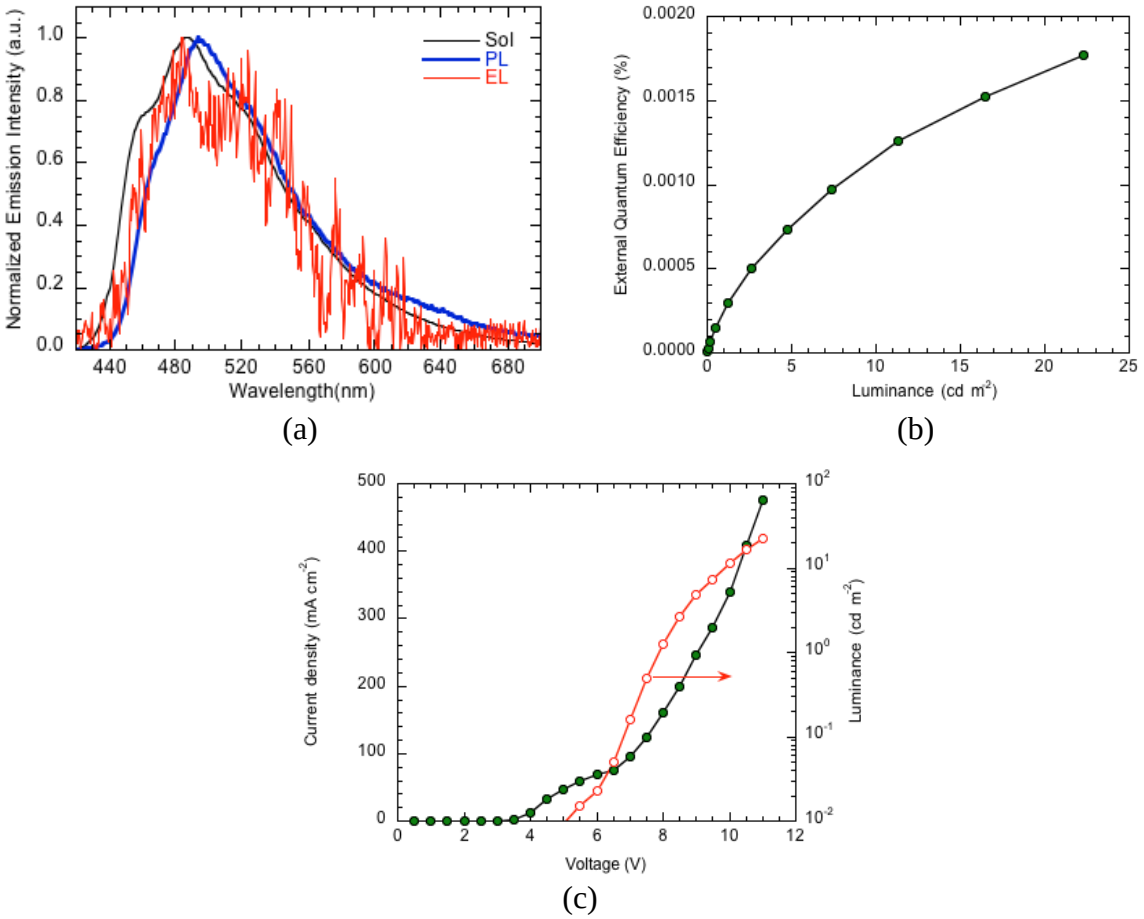

Figure S14. Characteristics of the ITO/PEDOT:PSS/**4c**/LiF/Al OLED: (a) electroluminescence spectrum (EL) compared with the spin coated neat film photoluminescence (PL) and solution fluorescence spectra in THF (Sol); (b) External Quantum Efficiency (EQE) *vs* Luminance; and (c) Current density (filled symbols)/Luminance (open symbols) *vs* Voltage.

Among the OLEDs based on neat complexes **4c**-**4f**, deposited by spin coating, a maximum luminance (L_{max}) of 33 cd m^{-2} was obtained for the **4f**-based OLED, with a maximum external quantum efficiency (EQE_{max}) of 1×10^{-3}%.

A group of devices based on films of complexes **4c**, **4d** and **4g** deposited by thermal vacuum deposition, with the structure: ITO (100 nm)/PEDOT:PSS (40 nm)/TPD (20 nm)/Complex (*ca.* 80 nm)/Bphen (11 nm)/LiF (1.5 nm)/Al (80 nm) was fabricated and characterized (Table S6).

Table S6. Characteristics of OLED devices based on vacuum thermal deposited complexes **4c**, **4d** and **4g** including maximum luminance (L_{max}, cd m^{-2}), external quantum efficiency (EQE_{max}, %), current efficiency (η_L, cd A^{-1}), and Commission Internationale de l'Éclairage (CIE) colour coordinates.

Complex	X	L_{max}	EQE_{max}	$\eta_{L_{max}}$	CIE
		ITO/PEDOT:PSS/TPD/Complex/Bphen/LiF/Al			
4c	4-Cl	1812	1.5×10^{-1}	4.9×10^{-1}	0.30, 0.51
4d	4-Br	488	3×10^{-2}	1.2×10^{-1}	0.33, 0.53
4g	2-Br	4	6×10^{-3}	1.2×10^{-2}	0.29, 0.38

It is worth pointing out that for OLEDs based on all three complexes, **4c**, **4d** and **4g**, the maximum emission is red shifted with respect to PL emission of the corresponding sublimed films (Figure S15).

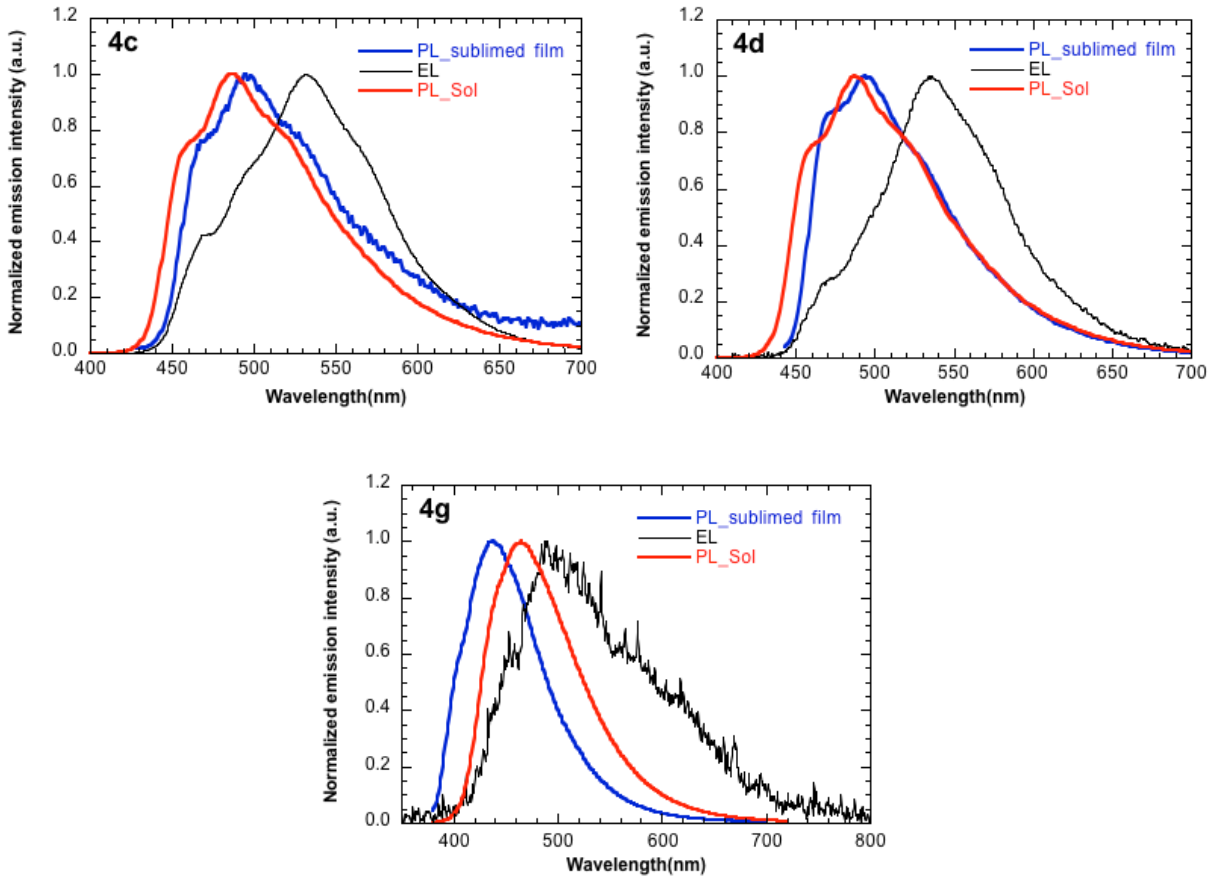

Figure S15. Comparison of **4c**, **4d** and **4g** emission spectra: electroluminescence (EL), sublimed film photoluminescent (PL) and solution fluorescence spectra in THF (Sol).

It is not clear whether this emission is related to an electrical current-driven degradation or due to an excited state that is of a different origin of that generated upon photoexcitation of the neat films.

Like the previous results, complexes **4c** and **4d** gave the best OLED performances, **4c** being the one exhibiting the higher luminance and EQE maxima (1812 cd m^{-2} and 0.15%, respectively). The characteristics of the device fabricated with **4c** by vacuum thermal deposition are shown in Figure S16.

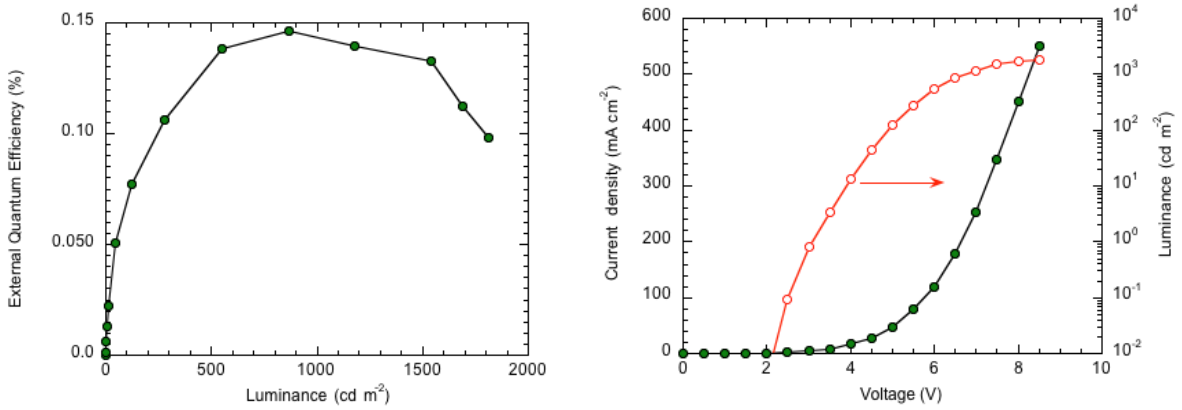

(a) (b)

Figure S16. Characteristics of the ITO/PEDOT:PSS/TPD/**4c**/Bphen/LiF/Al OLED: (a) External Quantum Efficiency (EQE) *vs* Luminance; and (b) Current density (filled symbols)/Luminance (open symbols) *vs* Voltage.

Complexes **4b**-**4g** were also dispersed in poly(vinylcarbazole) (PVK), a well-known hole-conducting polymer, in a 4% by weight concentration. OLEDs based on such blends, having the structure ITO/PEDOT:PSS/polyTPD/PVK+Complex(4%)/Ca/Al, were fabricated and characterized. The thicknesses of the emissive layer (PVK+Complex) were in the range 50-110 nm. The results of their characterization are shown in Table S7.

Table S7. Characteristics of OLEDs based on complexes **4b**-**4g** dispersed in PVK, ITO/PEDOT:PSS/polyTPD/PVK+Complex(4%)/Ca/Al, including maximum luminance (L_{max}, cd m^{-2}), external quantum efficiency (EQE_{max}, %), current efficiency ($\eta_{L_{max}}$, cd A^{-1}), and Commission Internationale de l'Éclairage (CIE) colour coordinates.

Complex	X	L_{max}	EQE_{max}	$\eta_{L_{max}}$	CIE
4b	4-F	75	4.1×10^{-3}	9.5×10^{-3}	0.19, 0.33
4c	4-Cl	21	1.3×10^{-3}	3.4×10^{-3}	0.21, 0.40
4d	4-Br	63	7.9×10^{-3}	2.6×10^{-3}	0.29, 0.51
4e	4-I	147	4.8×10^{-3}	1.6×10^{-2}	0.30, 0.53
4f	3-Br	20	7×10^{-4}	1.7×10^{-3}	0.28, 0.37
4g	2-Br	66	4.6×10^{-3}	1.2×10^{-2}	0.31, 0.42

The OLED based on complex **4e** showed the highest maximum luminance (147 cd m^{-2}), while **4d** gave the OLED with the maximum EQE (7.9×10^{-3}%). Figure S17 compares the emission spectra (PL and EL) for the various complexes.

All devices showed an EL spectrum that either closely resembles the solid-state PL or, most commonly, is slightly red shifted. Such red shift indicates that the emissive state is different from the one originating PL, which, in addition, may be due to some degradation of the emissive material during the OLED driving. Therefore, we do not find clear evidence that the OLEDs emission, in particular for complexes **4e**-**4g** (whose phosphorescence spectra is sown in Figure 3), has phosphorescence contribution. We have particularly analysed the emission of **4g**-based OLEDs. We found, in various devices, based on the neat complex and on devices based on **4g** dispersed in PVK that the maximum emission occurs at *ca.* 500 nm. There is also a shoulder around 620 nm that varies in intensity as shown in Figure S18. These characteristics can be due to either a phosphorescence contribution or degradation. Thereby we cannot confidently conclude that **4g** OLEDs exhibit phosphorescence emission.

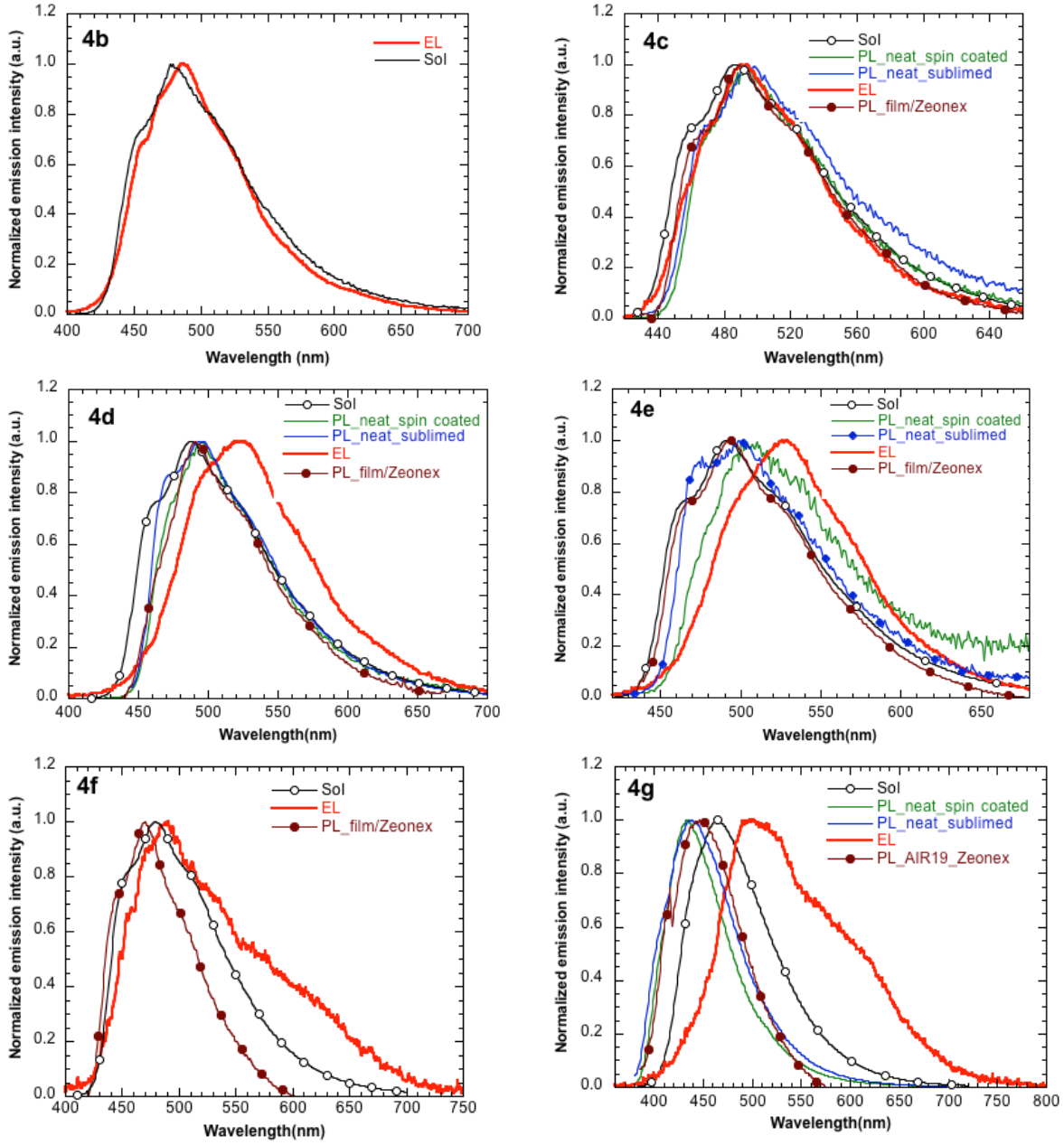

Figure S17. Comparison of solution fluorescence spectra (Sol), OLEDs emission spectra (EL) and films photoluminescence (PL) for the various complexes used in the fabrication of OLED with an active layer made of their blends with PVK.

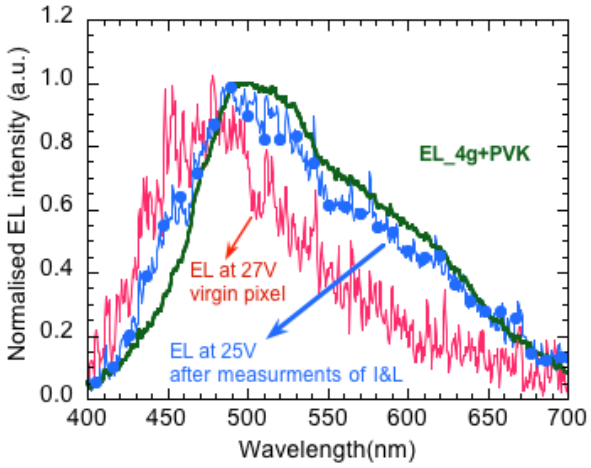

Figure S18. Comparison of the EL spectra recorded from an ITO/pedot/TPD/**4g**(sublim)/ Bphen/LiF/Al OLED for a pixel for which the Current and Luminance vs voltage output had been obtained up to 25 V (in blue), with the emission of a virgin pixel upon application of 27 V (in red). Also shown is the EL spectrum of the OLED ITO/polyTPD/PVK+**4g**/Ca/Al (in green).